

# Magnesiated Si-Rich $\text{SiO}_x$ Materials for High-Performance Lithium-Ion Batteries

Hyunsik Yoon, Ji Young Kim, Min Gyu Kim, and Hansu Kim\*

Silicon monoxide ( $\text{SiO}$ )-based materials have significant potential as high-capacity anode materials for lithium-ion batteries (LIBs). However, the low initial Coulombic efficiency (ICE) associated with the irreversible electrochemical reaction of the amorphous  $\text{SiO}_2$  phase ( $\text{a-SiO}_2$ ) in  $\text{SiO}$  hinders its application in commercial LIBs. The preemptive phase transition of  $\text{a-SiO}_2$  to an inactive silicate phase using a metal hydride is a promising strategy for improving the ICE. However, this process inevitably leads to reversible capacity loss. In this study, a high-capacity Si-rich  $\text{SiO}_x$  composite prepared by high-energy mechanical milling is premagnesiated

using  $\text{MgH}_2$ , resulting in a significantly improved capacity and ICE compared to those of pristine  $\text{SiO}$  and Si-rich  $\text{SiO}_x$  composites. The resulting  $\text{Si/Mg}_2\text{SiO}_4$  composite electrode exhibited a high initial discharge capacity of  $1961 \text{ mAh g}^{-1}$  with a high ICE of 87.0% and maintained highly stable capacity retention after 200 cycles compared to the Si-rich  $\text{SiO}_x$ . These improved electrochemical properties are attributed to the preemptively synthesized  $\text{Mg}_2\text{SiO}_4$ , which not only prevents irreversible reactions between lithium and  $\text{a-SiO}_2$  during the initial lithiation but also acts as a buffer phase that effectively reduces volume expansion during cycling.

## 1. Introduction

The rapid growth of electric vehicle (EV) and large-scale energy storage system (ESS) industries has led to an increased demand for lithium-ion batteries (LIBs) with higher energy density, driving the need to replace the commonly used graphite anode materials for LIBs.<sup>[1–4]</sup> Although graphite has a limited capacity of  $372 \text{ mAh g}^{-1}$ , Si can store a much greater number of lithium ions, providing a theoretical capacity of  $\approx 3850 \text{ mAh g}^{-1}$ , making it a promising anode material for LIBs.<sup>[1,5–10]</sup> However, Si-based anode materials undergo a volume expansion of  $\approx 300\%$  during charging and discharging, leading to mechanical degradation of the material, the detachment of the electrode from the current collector, and the repeated formation and fracturing of the SEI layer during cycling, thereby causing capacity fading in the cells.<sup>[11–14]</sup> Silicon monoxide ( $\text{SiO}$ ), which has a lower capacity than Si but undergoes a lower volume expansion of 160% than Si, can better maintain the structural stability of the electrodes, thus prompting significant research interest.<sup>[7,8,10,15]</sup> Nevertheless, some challenges must be addressed for the successful use of

$\text{SiO}$ -based anode materials in LIBs. A key issue is the poor initial Coulombic efficiency (ICE) of  $\text{SiO}$ -based anode materials owing to the irreversible reaction between the amorphous  $\text{SiO}_2$  phase ( $\text{a-SiO}_2$ ) in  $\text{SiO}$  and lithium upon the first lithiation to irreversibly form  $\text{Li}_2\text{O}$  and lithium silicates ( $\text{Li}_2\text{SiO}_3$ ,  $\text{Li}_4\text{SiO}_4$ ).<sup>[7,15–18]</sup> To improve the ICE of  $\text{SiO}$ -based anode materials, the introduction of other elements such as Li, C, and Mg, based on the Ellingham diagram, is used for a preemptive reaction with the  $\text{a-SiO}_2$  phase in  $\text{SiO}$  to form irreversible metal silicate phases.<sup>[19–23]</sup> Magnesium is also considered a promising candidate for improving the ICE of  $\text{SiO}$ -based anode materials.<sup>[24,25]</sup> Premagnesiation using Mg metal can improve the ICE of  $\text{SiO}$  through the preventive reaction of Mg with the  $\text{a-SiO}_2$  phase in  $\text{SiO}$  to form magnesium silicate.<sup>[26]</sup> However, the exothermic reaction between Mg and  $\text{SiO}$  causes a sudden temperature rise up to  $1941^\circ\text{C}$ , leading to the coarsening of the active Si phase.<sup>[20,25,27–29]</sup> Given that the size of active Si phase is key to the long-term cycle performance of Si-based anode materials,<sup>[28–30]</sup> a meticulous design of the magnesiation of  $\text{SiO}$  is crucial to avoid Si coarsening. Recently, our group reported that  $\text{MgH}_2$  instead of Mg, effectively suppressed the sudden temperature rise by exploiting the endothermic dehydrogenation reaction of  $\text{MgH}_2$  during  $\text{H}_2$  desorption, reducing the size of the active Si phase compared to that of Mg.<sup>[31]</sup> Although premagnesiation improves the ICE of the  $\text{SiO}$  anode material, a critical drawback is the inevitable decrease in the specific capacity of preemptive irreversibly phase-formed  $\text{SiO}$ -based materials compared to that of pristine  $\text{SiO}$ .<sup>[19,27,32]</sup> In this study, Si-rich  $\text{SiO}_x$  ( $0 < x < 1$ ), which has a higher specific capacity than  $\text{SiO}$ , was employed as the starting material for premagnesiation. Yang et al. reported that a  $\text{Si}_x\text{O}$  composite ( $x$  close to 2) prepared by high-energy mechanical milling (HEMM) of Si nanoparticles and  $\text{SiO}$  particles with a molar ratio of 2 (Si: $\text{SiO}$ ) delivered a much higher reversible capacity of  $2157 \text{ mAh g}^{-1}$  than  $\text{SiO}$ .<sup>[33]</sup> Cao et al. reported that  $\text{SiO}_{0.37}$  prepared by ball-milling Si powder in air,

H. Yoon, M. G. Kim, H. Kim

Department of Battery Engineering

Hanyang University

222 Wangsimni-ro, Seongdong-gu, Seoul 04763, Republic of Korea

J. Y. Kim, H. Kim

Department of Energy Engineering

Hanyang University

222 Wangsimni-ro, Seongdong-gu, Seoul 04763, Republic of Korea

E-mail: khansu@hanyang.ac.kr



Supporting information for this article is available on the WWW under <https://doi.org/10.1002/batt.202500473>



© 2025 The Author(s). *Batteries & Supercaps* published by Wiley-VCH GmbH. This is an open access article under the terms of the Creative Commons Attribution License, which permits use, distribution and reproduction in any medium, provided the original work is properly cited.

delivered a volumetric capacity of  $1800 \text{ Ah L}^{-1}$ .<sup>[34]</sup> However, it is well recognized that the cycle performance of Si-rich  $\text{Si}_x\text{O}$  ( $x$  is more than 1) diminishes as the relative amount of active Si phase in the  $\text{SiO}_x$  composite increases.<sup>[35–38]</sup> We anticipated that premagnesiated Si-rich  $\text{SiO}_x$  would not only show a higher specific capacity than premagnesiated SiO but also better capacity retention compared to bare Si-rich  $\text{SiO}_x$ , mainly because of the Li-inactive magnesium silicate phase formed by premagnesiation. As a result, premagnesiated Si-rich  $\text{SiO}_x$  delivered a higher discharge capacity of  $1961 \text{ mAh g}^{-1}$  than premagnesiated SiO with an ICE of 87% and a significantly improved capacity retention compared to as-prepared porous Si-rich  $\text{SiO}_x$ .

## 2. Results and Discussion

**Figure 1a** shows a schematic of the preparation of porous  $\text{Si}/\text{Mg}_2\text{SiO}_4$  composite materials. Si rich Si/SiO composites, denoted  $\text{SiO}_{0.5}$ , were prepared by HEMM of a mixture consisting of micron-sized Si and SiO particles in a 1:1 molar ratio, followed by magnesiation process using  $\text{MgH}_2$ . According to the random mixture model of amorphous SiO, we assumed that amorphous SiO was a random mixture composed of amorphous Si phase (a-Si) and a- $\text{SiO}_2$ .<sup>[39,40]</sup> Magnesiation of  $\text{SiO}_{0.5}$  using  $\text{MgH}_2$  was performed to improve the electrochemical performance of  $\text{SiO}_{0.5}$  by the preemptive formation of the  $\text{Mg}_2\text{SiO}_4$  phase through

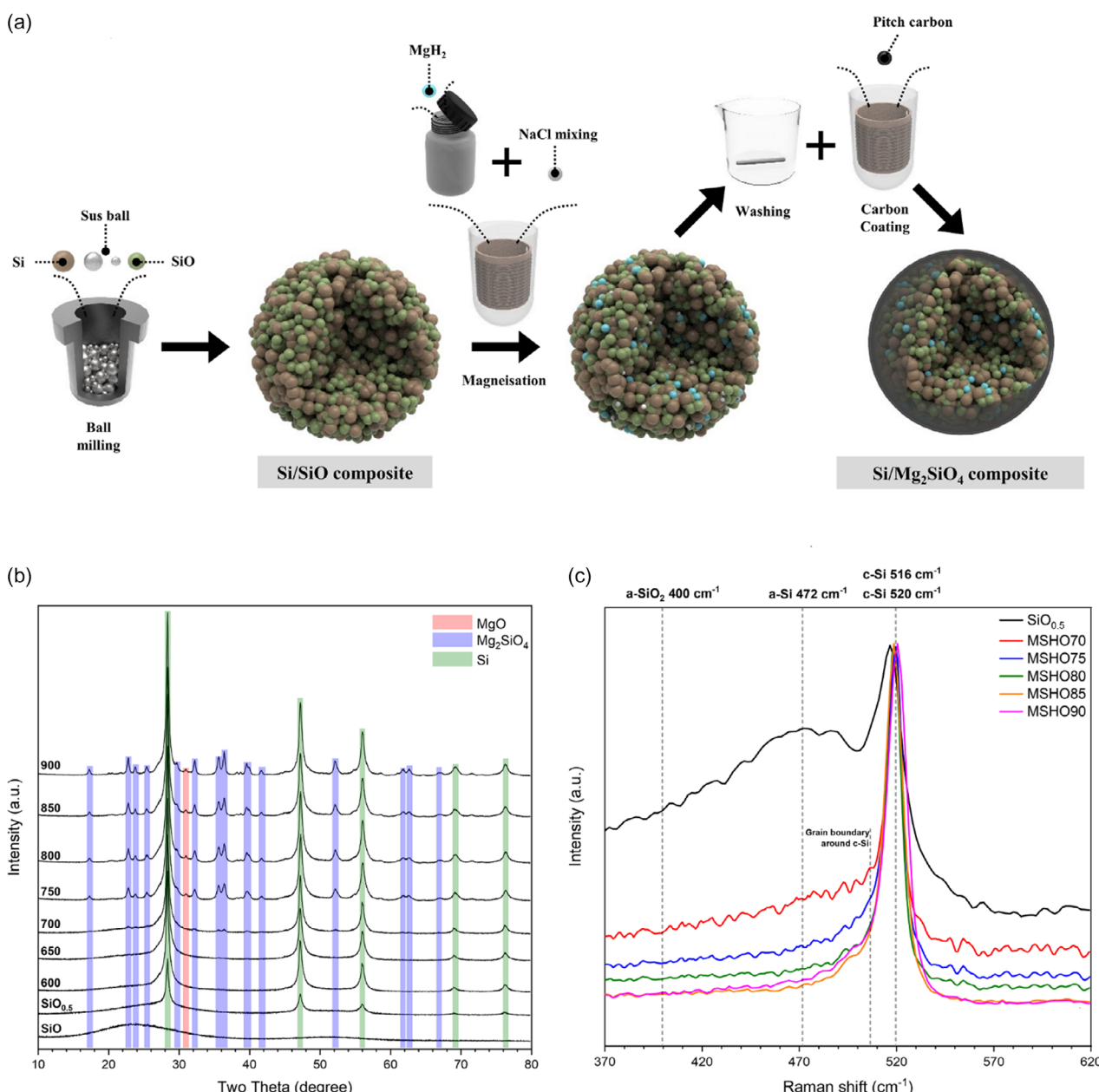


**Figure 1.** a) Schematic illustration of the synthesis process for  $\text{Si}/\text{Mg}_2\text{SiO}_4$  composite, including HEMM of  $\text{Si}/\text{SiO}$  composite, magnesiation using  $\text{MgH}_2$ , followed by acetic acid washing and carbon coating. b) XRD patterns of  $\text{SiO}$ ,  $\text{SiO}_{0.5}$ , and  $\text{Si}/\text{Mg}_2\text{SiO}_4$  composites synthesized at different heat treatment temperatures. c) Raman spectra for  $\text{SiO}_{0.5}$ , MSHO70, MSHO75, MSHO80, MSHO85, and MSHO90.

the reaction between  $\text{MgH}_2$  and a-SiO<sub>2</sub> in SiO<sub>0.5</sub>, as shown in Equation (1)



According to our previous work on the magnesiation of SiO with MgH<sub>2</sub>, the Mg/Si molar ratio was set to be 0.5 for magnesiation with the help of NaCl, which was also introduced as a thermal moderator prior to the magnesiation of SiO<sub>0.5</sub>.<sup>[31,41]</sup> After the magnesiation, the obtained powders were washed with an acetic acid solution to remove NaCl, followed by carbon coating to enhance electrical conductivity, and denoted as magnesiated silicon half oxide (MSHO). Figure 1b shows X-ray diffraction (XRD) patterns of magnesiated SiO<sub>0.5</sub> at various heat-treatment temperatures from 600 to 900 °C, denoted as MSHO60, MSHO65, MSHO70, MSHO75, MSHO80, MSHO85, and MSHO90, respectively. The XRD pattern of SiO<sub>0.5</sub> showed Bragg peaks for crystalline Si with a broad peak corresponding to amorphous SiO, indicating that SiO<sub>0.5</sub> consisted of crystalline Si and amorphous SiO. The XRD patterns of MSHO60 and MSHO65 were almost identical to those of SiO<sub>0.5</sub>. On the other hand, XRD patterns of SiO<sub>0.5</sub> magnesiated at temperatures above 700 °C show Bragg peaks for Mg<sub>2</sub>SiO<sub>4</sub>, as well as those for crystalline Si phase (c-Si). These results clearly showed that magnesiation of SiO<sub>0.5</sub> was successfully performed at temperatures higher than 700 °C, as intended. The XRD patterns of MSHO75, MSHO80, MSHO85, and MSHO90 also show a weak Bragg peak for the MgO phase, which may have been formed by the exposure of MgH<sub>2</sub> to oxygen in air.<sup>[31]</sup> Figure 1c shows the Raman spectra of the SiO<sub>0.5</sub> and magnesiated SiO<sub>0.5</sub> samples at various heat-treatment temperatures. The Raman spectrum of SiO<sub>0.5</sub> shows two broad Raman bands at 400 and 472 cm<sup>-1</sup>, corresponding to the a-SiO<sub>2</sub> and a-Si phases, respectively, and a sharp Raman band at 516 cm<sup>-1</sup> corresponding to c-Si.<sup>[42,43]</sup> The observed bands corresponding to the a-SiO<sub>2</sub> and a-Si phases originated from the SiO particles, whereas the band for c-Si originated from the Si particles. We found that the band for the c-Si phase in the Raman spectrum of SiO<sub>0.5</sub> was slightly shifted from 520 cm<sup>-1</sup>. Such a band shift toward lower wavenumbers, accompanied by an increase in the bandwidth, can be attributed to the changes in the Si–Si bond length caused by the HEMM process,<sup>[44,45]</sup> which changed the band position and caused a larger variation in the distribution of bond lengths, contributing to the broader peak width. The Raman spectrum of MSHO70 also showed weakened Raman bands for SiO with the band for c-Si at 520 cm<sup>-1</sup>. In contrast, the Raman spectra observed for the samples treated above 750 °C showed only the Raman band for c-Si without any band for amorphous SiO.<sup>[43]</sup> These results suggest the full magnesiation of SiO<sub>0.5</sub> at 750 °C, which is well matched with XRD analysis.

Figure 2a shows the voltage profiles of the as-prepared SiO<sub>0.5</sub>, carbon-coated SiO<sub>0.5</sub> (C-SiO<sub>0.5</sub>), and MSHO electrodes in the first cycle. As shown in Figure 2a,b, the SiO<sub>0.5</sub> electrode delivered a discharge capacity of 2156 mAh g<sup>-1</sup> with an ICE of 71.1%. Carbon coating of SiO<sub>0.5</sub> slightly improved the discharge capacity to

2306 mAh g<sup>-1</sup> with a higher ICE of 79.5% than the as-prepared SiO<sub>0.5</sub> electrode.<sup>[46,47]</sup> As expected, the MSHO electrodes showed initial discharge capacities of 1842 mAh g<sup>-1</sup> (MSHO70), 1836 mAh g<sup>-1</sup> (MSHO75), 1961 mAh g<sup>-1</sup> (MSHO80), 1710 mAh g<sup>-1</sup> (MSHO85), and 1657 mAh g<sup>-1</sup> (MSHO90), which were much higher than those of previously reported premagnesiated SiO (1108 mAh g<sup>-1</sup>).<sup>[31]</sup> Premagnesiation significantly improved the ICE of the MSHO electrodes: 82.5% for MSHO70, 86.3% for MSHO75, 87.0% for MSHO80, 86.7% for MSHO85, and 84.9% for MSHO90. Among the premagnesiated SiO<sub>0.5</sub> electrodes, the MSHO80 electrode exhibited the highest discharge capacity and ICE. Figure 2c shows the differential capacity plots (DCP) of the SiO<sub>0.5</sub> and MSHO electrodes at various magnesiation temperatures for the first cycle. The DCP of the SiO<sub>0.5</sub> electrode showed broad anodic peaks at 270 mV (vs. Li/Li<sup>+</sup>) and sharp anodic peaks at 430 mV (vs. Li/Li<sup>+</sup>). The observed anodic peaks are associated with the dealloying reaction of the a-Li<sub>x</sub>Si phase and the delithiation of the Li<sub>15</sub>Si<sub>4</sub> phase.<sup>[48,49]</sup> The SiO<sub>0.5</sub> electrode also showed a broad cathodic peak at ≈180 mV (vs. Li/Li<sup>+</sup>), reflecting the irreversible reaction of the a-SiO<sub>2</sub> phase in SiO with lithium to form lithium silicate (Li<sub>2</sub>SiO<sub>3</sub> and Li<sub>4</sub>SiO<sub>4</sub>).<sup>[17,49]</sup> In contrast, the MSHO electrode did not exhibit this cathodic peak at 180 mV (vs. Li/Li<sup>+</sup>), which could be attributed to the preemptive formation of the Mg<sub>2</sub>SiO<sub>4</sub> phase. Figure 2d,e show the cycle performances of the SiO<sub>0.5</sub> and MSHO electrodes from three formation cycles at a current density of 100 mA g<sup>-1</sup>, followed by 200 cycles at a current density of 500 mA g<sup>-1</sup>. The SiO<sub>0.5</sub> and MSHO70 electrodes showed poor capacity retention over 200 cycles (38.2% of their initial capacity after 200 cycles for SiO<sub>0.5</sub> and 23.0% for MSHO70). On the other hand, other MSHO electrodes showed improved capacity retention compared to the as-prepared SiO<sub>0.5</sub> electrode as well as the MSHO70 electrodes: 42.3% for MSHO75, 48% for MSHO80, 50.8% for MSHO85, and 40.5% for MSHO90. This enhanced capacity retention of the MSHO electrode may be attributed to the Li-inactive Mg<sub>2</sub>SiO<sub>4</sub> phase, which acts as a mechanical buffer against the severe volume changes of the active Si phase during cycling.

Figure 3a-d show top-view and cross-sectional images of the SiO<sub>0.5</sub>, and MSHO80 particles obtained by focused ion beam-scanning electron microscopy (FIB-SEM). Figure 3a,b show that the SiO<sub>0.5</sub> particles have a spherical shape with a rough surface, indicating that SiO<sub>0.5</sub> particles are composed of fractured and cold-welded Si and SiO particles. Figure 3c,d show that the MSHO80 particles have almost the same morphology as SiO<sub>0.5</sub> particles, indicating that the magnesiation process did not significantly alter the particle shape. Figure 3e-q show the high-resolution transmission electron microscopy (HR-TEM) images with selected area electron diffraction (SAED) patterns, high-angle annular dark-field scanning transmission electron microscopy (HAADF-STEM) images, and energy-dispersive X-ray spectroscopy (EDS) mapping of the SiO<sub>0.5</sub> and MSHO80 particles. Figure 3e shows an HR-TEM image of SiO<sub>0.5</sub> particles, where the c-Si phase ( $d_{111} = 3.13 \text{ \AA}$ ,  $d_{220} = 1.92 \text{ \AA}$ ,  $d_{311} = 1.63 \text{ \AA}$ ) was identified; Figure 3g shows the SAED patterns that further confirm the c-Si phase. Figure 3i shows the HAADF-STEM image of the SiO<sub>0.5</sub> particles, revealing two distinguishable domains based on the atomic number (Z) contrast: a bright domain

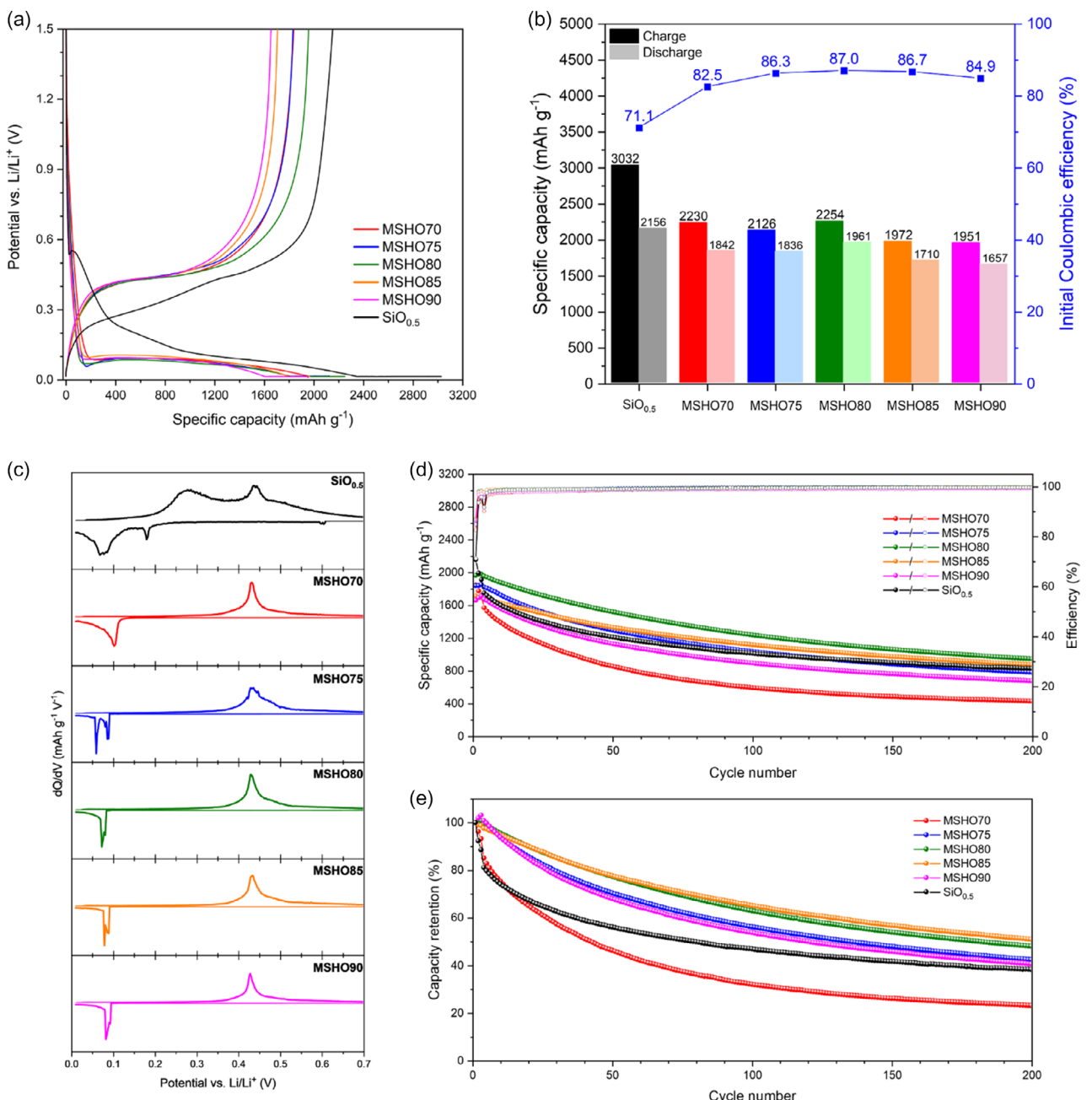


**Figure 2.** a) First cycle voltage profiles in the voltage range of 0.01–1.5 V versus Li/Li<sup>+</sup> at 100 mA g<sup>-1</sup>, b) gravimetric discharge/charge capacities and ICEs. c) DCP at the first cycle. d) Cycle performances and e) capacity retentions after three formation cycles at 100 mA g<sup>-1</sup>, followed by cycling at 500 mA g<sup>-1</sup> for SiO<sub>0.5</sub>, MSHO70, MSHO75, MSHO80, MSHO85, and MSHO90.

and a dark domain. Figure 3j–l shows the EDS map, where the red signal region marked with a circle is aligned with the bright domain. Magnified EDS mapping of the Si and O signals clearly shows a Si-rich bright domain without the O signal, which can be assigned to the fractured Si particles generated during the HEMM process. The HR-TEM image of another region with homogeneously distributed Si and O signals aligned with the dark domain showed a diffused ring pattern (Figure S1, Supporting Information). These results suggest that SiO<sub>0.5</sub> contained both c-Si and amorphous SiO with a uniform distribution of Si and

O atoms,<sup>[50]</sup> which is in good agreement with the XRD results. Figure 3f shows an HR-TEM image of MSHO80 particles, where the previously identified c-Si and newly emerged c-Mg<sub>2</sub>SiO<sub>4</sub> ( $d_{200} = 5.10 \text{ \AA}$ ) were identified; the corresponding SAED patterns further confirm the presence of c-Si and c-Mg<sub>2</sub>SiO<sub>4</sub> (Figure 3h). Figure 3m shows HAADF-STEM images of the MSHO80 particles, revealing two distinct domains based on the atomic number (Z) contrast: a bright domain and a dark domain. Figure 3n–q shows the EDS mapping of MSHO80, where the Si-rich bright domain and the O- and Mg-rich dark domain can be assigned to Si

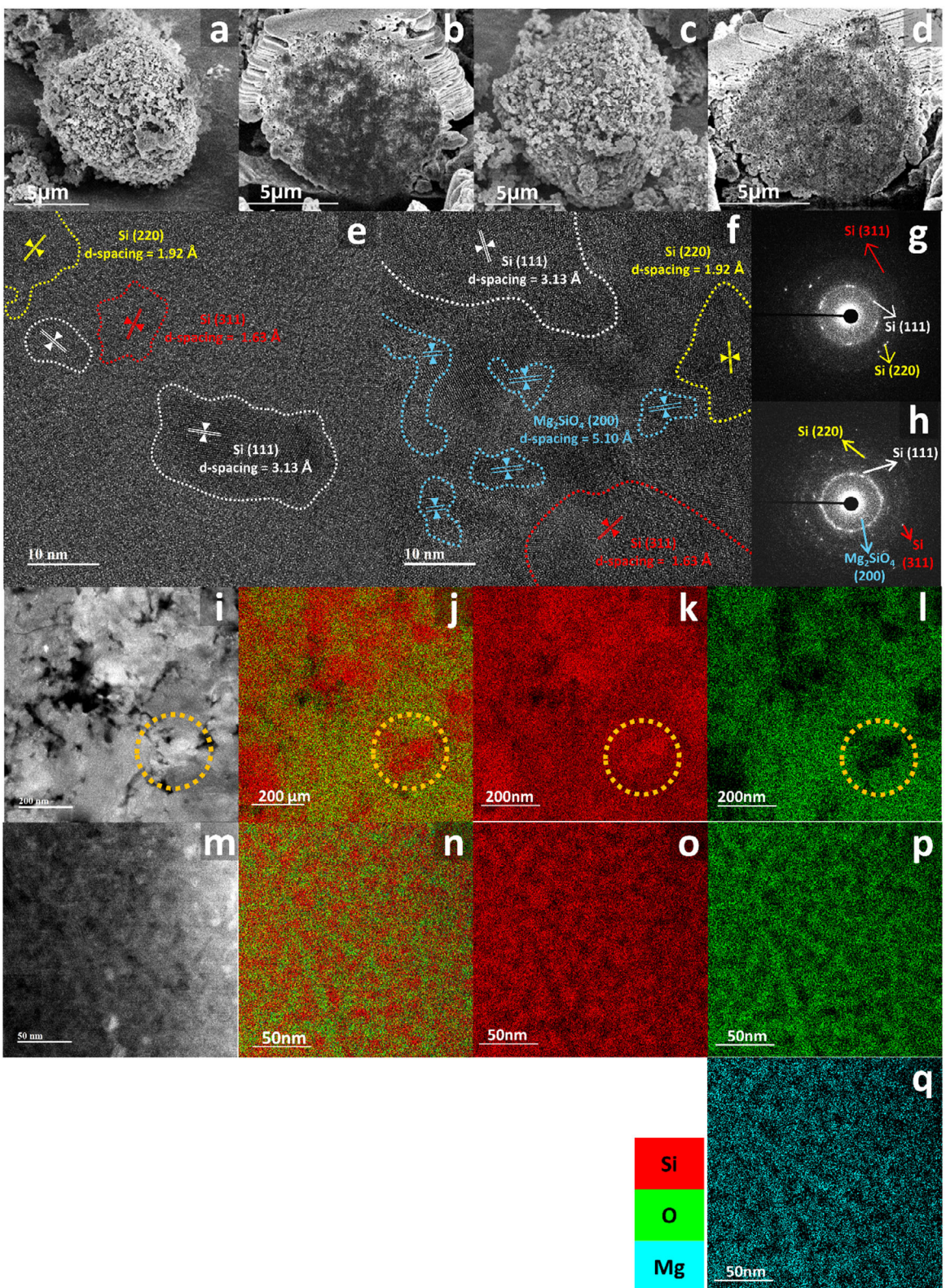


**Figure 3.** Top-view SEM images of a)  $\text{SiO}_{0.5}$  and c) MSHO80. Cross-sectional SEM images of b)  $\text{SiO}_{0.5}$  and d) MSHO80. HR-TEM and SAED patterns of e,g)  $\text{SiO}_{0.5}$  and f,h) MSHO80. HADDF-STEM and STEM-EDS mapping images of i-l)  $\text{SiO}_{0.5}$  (250 K) and m-q) MSHO80 (1 M). Red, green, and cyan marks in STEM-EDS represents the Si, O, and Mg, respectively.

and  $\text{Mg}_2\text{SiO}_4$ , respectively. The lower magnification of HAADF-STEM and EDS mapping of MSHO80 demonstrated the presence of fractured Si particles, even after magnesiation (Figure S2, Supporting Information). These observations suggest that the  $\alpha\text{-SiO}_2$  phase in  $\text{SiO}_{0.5}$ , transformed into  $\text{Mg}_2\text{SiO}_4$  through magnesiation whereas the Si region remained the same as that before. Unlike the Si region, SiO region underwent a phase transformation into  $\text{Si}/\text{Mg}_2\text{SiO}_4$ , and the Si domain size varied depending on the heat treatment temperature. Among the MSHO samples, MSHO80 showed the smallest Si domain size, as estimated from the Scherrer equation and STEM images, which might account for its enhanced cycle performance (Table S1 and Figure S3, Supporting Information).

**Figure 4a,b** show the cross-sectional SEM images and thickness changes of the  $\text{SiO}_{0.5}$  and MSHO80 electrodes after the initial discharge to 10 mV (vs. Li/Li<sup>+</sup>) after 1 cycle and after 200th cycles. The  $\text{SiO}_{0.5}$  electrode expanded by 117.6% after initial lithiation and contracted by 19.2% after 1 cycle. On the other hand, the MSHO80 electrode expanded by 36.9% after initial lithiation and contracted

by 4.1% after 1 cycle. The larger expansion and contraction of the  $\text{SiO}_{0.5}$  electrode during the initial cycles may be attributed to the irreversible formation of lithium silicate phases. In contrast, the MSHO80 electrode did not undergo this irreversible electrochemical reaction because of the preemptive formation of the  $\text{Mg}_2\text{SiO}_4$  phase via magnesiation of  $\text{SiO}_{0.5}$ . It should be noted that the MSHO80 electrode showed a much lower expansion rate of 80.7% after 200th cycles, which is a much suppressed value compared to that of the  $\text{SiO}_{0.5}$  electrode (226.2%) after 200th cycles. The significantly improved dimensional stability of the MSHO80 electrode compared to that of the  $\text{SiO}_{0.5}$  electrode explains the better capacity retention of the MSHO80 electrode compared to the  $\text{SiO}_{0.5}$  electrode. These results suggest that the  $\text{Mg}_2\text{SiO}_4$  phase may have acted as a buffer phase to ensure the mechanical integrity of MSHO80 against volume changes in the Si phase domain during cycling.

Coin-type full cells were investigated to compare MSHO80 and  $\text{SiO}_{0.5}$ , which were blended with graphite, as the negative electrodes. **Figure 5a** shows the voltage profiles of the coin-type full cells

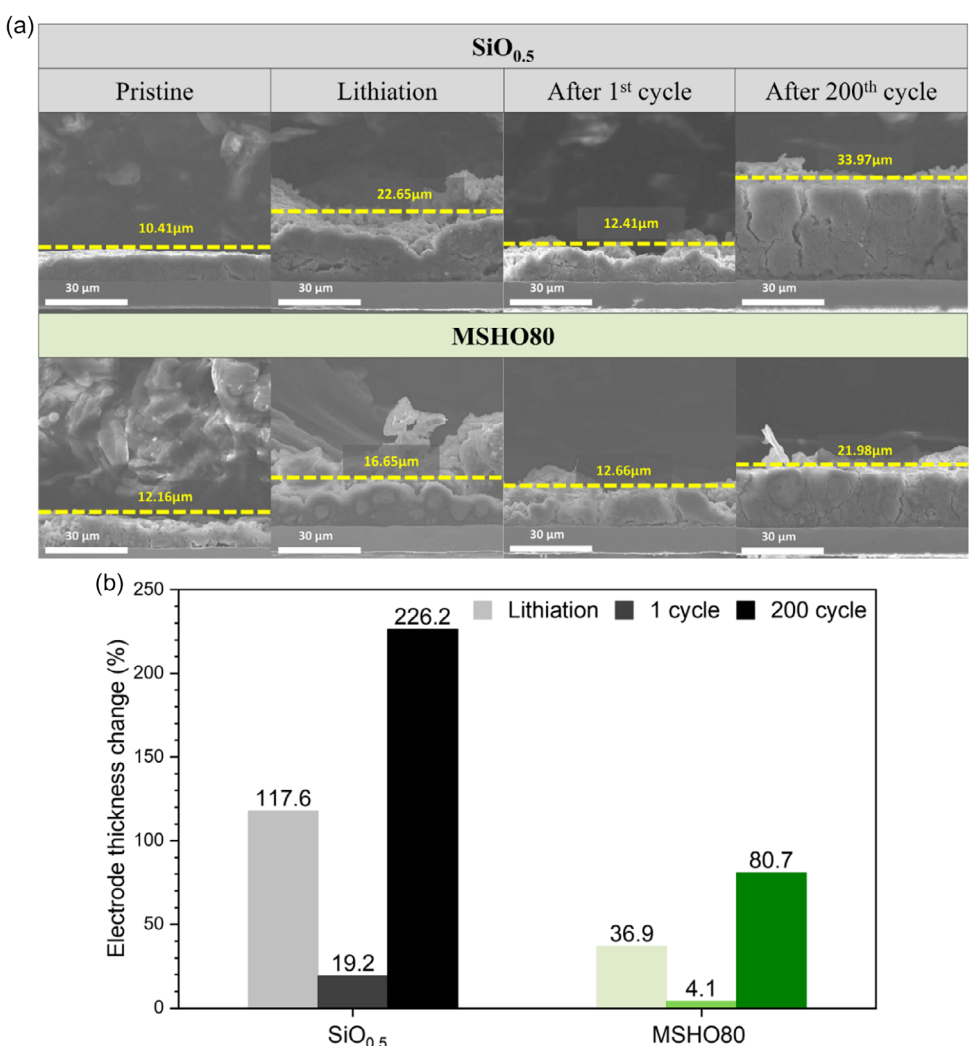


**Figure 4.** a) Cross-sectional SEM images of the  $\text{SiO}_{0.5}$ , MSHO80 electrode before cycling, after first lithiation, after first cycle, and after 200th cycles.  
b) Electrode thickness changes of the  $\text{SiO}_{0.5}$ , MSHO80 after first lithiation, after first cycle, and after 200th cycles.

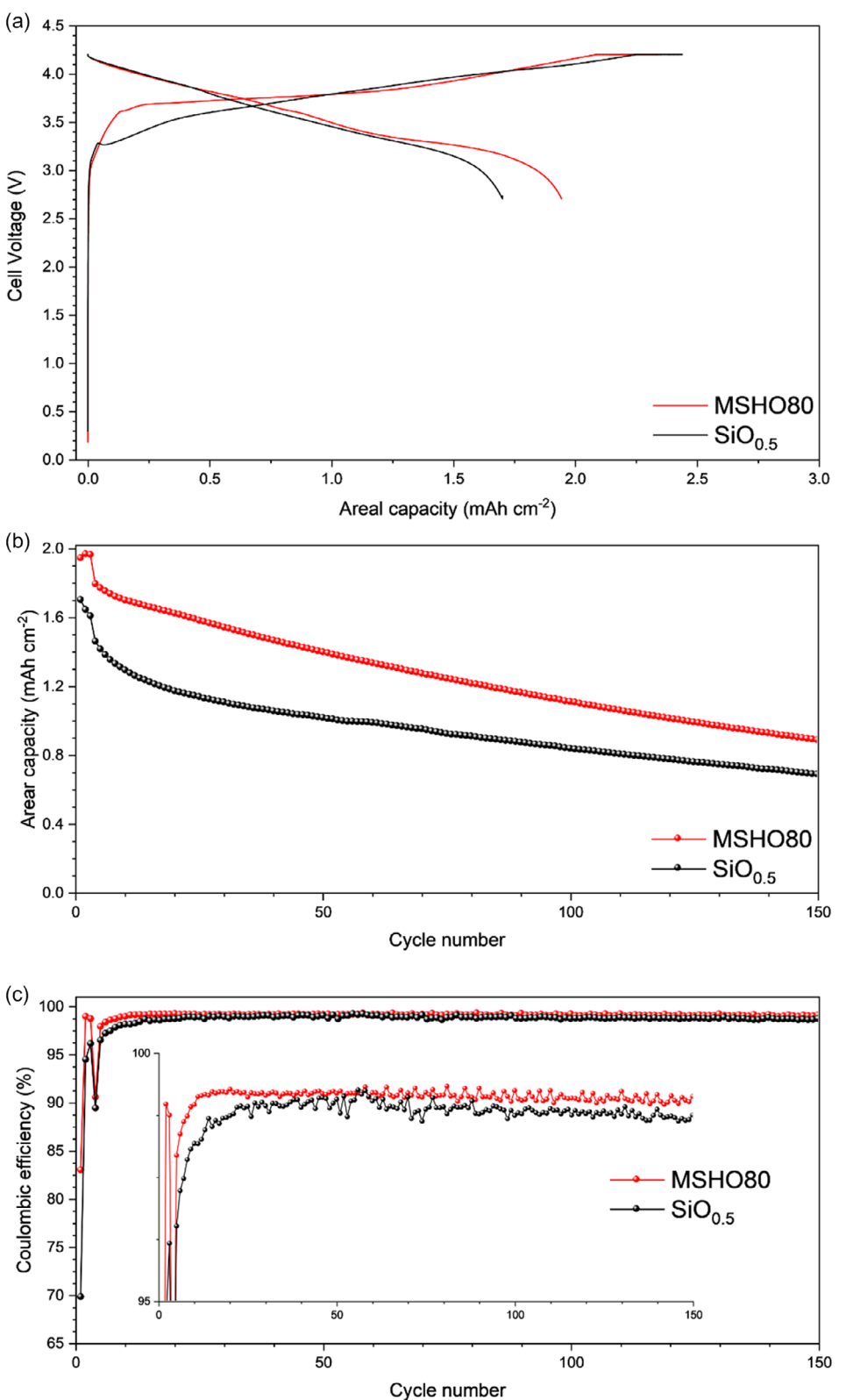


**Figure 5.** a) First cycle voltage profiles of  $\text{SiO}_{0.5}$  and MSHO80 based coin-type full cells in the voltage range of 2.7–4.2 V at 0.227 mA, b) discharge capacities, and c) Coulombic efficiency as a formation of the cycle number at 2.27 mA after three cycles at 1.135 mA for the prepared coin-type full cells.

adopting a  $\text{LiNi}_{0.5}\text{Co}_{0.2}\text{Mn}_{0.3}\text{O}_2$  cathode with MSHO-graphite and  $\text{SiO}_{0.5}$ -graphite anodes in the first cycle. The MSHO80 full cell showed an area capacity of  $1.94 \text{ mAh cm}^{-2}$  with an ICE of 83.0%, while the  $\text{SiO}_{0.5}$  full cell delivered an areal capacity of  $1.70 \text{ mAh cm}^{-2}$  with an ICE of 69.7%. Note that the charge capacity of the full cells was  $2.34 \text{ mAh cm}^{-2}$  for MSH80 full cell and  $2.44 \text{ mAh cm}^{-2}$  for  $\text{SiO}_{0.5}$  full cell. Given that the charge capacities of the full cells were similar, the difference in the discharge areal capacity of the full cells was mainly due to the higher ICE of MSHO80 than that of  $\text{SiO}_{0.5}$ . Figure 5b shows the cycle performance of the  $\text{SiO}_{0.5}$  and MSHO80 full cells. The MSHO80 full cell delivered a discharge capacity of  $0.894 \text{ mAh cm}^{-2}$  after 150 cycles, which was higher than that of the  $\text{SiO}_{0.5}$  full cell ( $0.694 \text{ mAh cm}^{-2}$ ). Figure 5c shows the coulombic efficiency of the coin-type full cell during cycling, which is also significant evidence of the stable capacity retention of the MSHO80 full cell. From the first to the 25th cycle, the MSHO80 full cell showed a higher average Coulombic efficiency of 98.03%, compared to that of the  $\text{SiO}_{0.5}$  full cell (96.60%). Over 150 cycles, MSHO80 full cell maintained an average Coulombic efficiency of 98.95%, which was also slightly higher than that of the  $\text{SiO}_{0.5}$  full cell (98.49%). Considering the suppressed volume expansion of the MSHO80 electrode compared to that of the  $\text{SiO}_{0.5}$  electrode during cycling, the  $\text{Mg}_2\text{SiO}_4$  inactive phase is key to maintaining the initial capacity during cycling.

### 3. Conclusion

This study proposes a solution to the capacity loss problem associated with ICE improvement by premagnesiation of SiO anode materials. We synthesized a Si-rich Si/SiO composite for high-capacity materials using HEMM followed by magnesiation with  $\text{MgH}_2$  to improve the ICE of the Si-rich Si/SiO composites. A preemptive reaction of the  $\alpha\text{-SiO}_2$  phase in the Si-rich Si/SiO composite with Mg released from dehydrogenated  $\text{MgH}_2$  formed a Li-inactive  $\text{Mg}_2\text{SiO}_4$  phase, resulting in the successful preparation of the Si/ $\text{Mg}_2\text{SiO}_4$  composite. The resulting Si/ $\text{Mg}_2\text{SiO}_4$  composite electrode showed a high capacity of  $1961 \text{ mAh g}^{-1}$  and a high ICE of 87.0%. The high-capacity Si-rich starting material effectively compensated for the inevitable capacity loss caused by the preemptive formation of the Li-inactive  $\text{Mg}_2\text{SiO}_4$  phase, which improved the ICE. This study provides valuable insights into the development of high-performance SiO anode materials for LIBs.

## 4. Experimental Section

### Material Preparation

To synthesize the  $\text{SiO}_{0.5}$  composites, commercial silicon (Alfa Aesar, USA) and SiO (OSAKA Titanium Tech. Co. Ltd., Japan) powders were dry-milled in a 1:1 molar ratio using a vibratory ball mill operating at 800 rpm for 27 h under an argon environment, with a ball-to-powder weight ratio (BPR) of 21:1 using a stainless steel (SUS) container and SUS balls. A 5 g portion of the milled powder was subsequently blended with magnesium hydride ( $\text{MgH}_2$ , >98%, American Elements) powder using a paint shaker in an argon-filled vessel. The Mg-to-Si molar ratio

was controlled at 0.25. This precursor mixture was then homogenized with 5 g of high-purity NaCl (>99.0%, Sigma-Aldrich) using an agate mortar within an argon glove box. The resulting blend was placed into an alumina crucible, with an additional 3.5 g NaCl layer applied on top to assist in thermal buffering and uniform reaction. Heat treatment was conducted at selected temperatures (600–900 °C, in 50 °C increments) for 5 h in a vertical tube furnace under argon, using a ramp rate of  $5 \text{ °C min}^{-1}$ . Each sample is denoted MSHOxx, where xx refers to the reaction temperature (e.g., MSHO80 for 800 °C). Postreaction, the powders were immersed in a 0.1 M acetic acid solution with magnetic stirring at 400 rpm for 30 min at room temperature to remove byproducts. The etched composites were filtered and vacuum-dried at 80 °C. To enhance electrical conductivity, carbon coating was performed on the surface of the composite particle to form carbon layer by mixing the powders with coal tar pitch (Posco Chemical Co. Ltd., Korea) in a 9:1 weight ratio (10 wt%), followed by thermal treatment at 800 °C for 2 h under argon with the same heating rate.

### Material Characterization

XRD patterns were recorded using a Bruker D8 Advance diffractometer with Cu K $\alpha$  radiation ( $\lambda = 1.5406 \text{ \AA}$ ) to identify the crystalline phases of the synthesized composites. Raman spectra of both Si/ $\text{Mg}_2\text{SiO}_4$  and pristine Si/SiO materials were obtained using a Thermo Fisher DXR3xi spectrometer with a 532 nm laser excitation. Morphological features and elemental compositions were examined using field-emission scanning electron microscopy (FE-SEM; Nova Nano SEM200, FEI) and EDS. For internal structural imaging, focused ion beam (FIB) milling was conducted followed by cross-sectional SEM and EDS analysis. Further microstructural evaluation was performed using HR-TEM, HAADF-STEM, and EDS mapping with a NEO ARM instrument (JEOL, Japan).

### Electrochemical Characterization

Electrode slurries were formulated by dispersing the active composite, polyacrylic acid binder (2 wt% in water, Sigma-Aldrich), and Super-P conductive carbon (TIMCAL) in an 8:1:1 mass ratio. The slurries were uniformly cast onto copper foil, targeting an active material loading of  $\approx 0.6 \text{ mg cm}^{-2}$ , and dried in a vacuum oven at 120 °C for 2 h. Electrochemical performance was evaluated using CR2032 coin cells with lithium metal as the counter electrode. Galvanostatic cycling was carried out in constant current–constant voltage (CC–CV) mode between 0.01 and 1.5 V (vs. Li/Li $^+$ ). Initial cycling (three cycles) was conducted at  $100 \text{ mA g}^{-1}$ , followed by prolonged cycling at  $500 \text{ mA g}^{-1}$  for 200 cycles. The voltage hold in CV mode was applied at 10 mV with a cutoff current of  $10 \text{ mA g}^{-1}$ . Discharge steps were executed in constant current mode under the same voltage window.

### Coin-Type Full Cell Measurement

Full cells were fabricated using negative electrodes composed of 77.25 wt% commercial graphite blended with 18 wt% active composite (either  $\text{SiO}_{0.5}$  or MSHO80), 1.25 wt% Super-C (TIMCAL) as the conductive agent, and a multibinder system comprising 1.0 wt% styrene-butadiene rubber (BM-400B, Zeon), 0.75 wt% carboxymethyl cellulose (CMC; Dai-ichi Kogyo Seiyaku), and 1.75 wt% polyacrylic acid (PAA). These slurries were cast onto Cu foil to achieve an areal capacity of  $2.24 \text{ mAh cm}^{-2}$ . The cathodes were prepared by coating a slurry containing 94 wt%  $\text{LiNi}_{0.5}\text{Co}_{0.2}\text{Mn}_{0.3}\text{O}_2$  (NMC), 3 wt% Super-P, and 3 wt% polyvinylidene fluoride (PVDF; Kureha Corporation) onto Al foil, with a loading of  $13.09 \text{ mg cm}^{-2}$  corresponding to an areal capacity of  $2.0 \text{ mAh cm}^{-2}$ . Both electrodes were dried in vacuum

at 200 °C for 2 h prior to assembly. CR2032-type full cells were assembled in an argon-filled glove box using polyethylene separators (F16BME, Tonen, Japan) and an electrolyte composed of 1.0 M LiPF<sub>6</sub> in EC/EMC/DEC (2:2:5 v/v/v) with 10 wt% fluoroethylene carbonate (FEC). Charge–discharge tests were conducted in CC–CV mode between 2.7 and 4.2 V. Formation cycling (first three cycles) was conducted at 0.1C (0.227 mA), followed by long-term cycling at 0.5C (1.135 mA) for 150 cycles.

## Supporting Information

The authors have cited additional references within the Supporting Information

## Acknowledgements

This work was supported by the National Research Foundation of Korea (NRF), grant funded by the Korean government (MSIT) (NRF- 2021M3H4A1A02045967).

## Conflict of Interest

The authors declare no conflict of interest.

## Author Contributions

**Hyunsik Yoon:** conceptualization (lead); investigation (lead); writing—original draft (lead); writing—review & editing (lead).  
**Ji Young Kim:** conceptualization (supporting); investigation (supporting). **Min Gyu Kim:** investigation (supporting); methodology (supporting). **Hansu Kim:** project administration (lead); supervision (lead); writing—original draft (lead); writing—review & editing (lead).

## Data Availability Statement

The data that support the findings of this study are available in the supplementary material of this article.

**Keywords:** high capacity · initial coulombic efficiency · lithium-ion batteries · premagnesiation · SiO

- [1] J. W. Choi, D. Aurbach, *Nat. Rev. Mater.* **2016**, *1*, 16013.
- [2] G. Jeong, Y.-U. Kim, H. Kim, Y.-J. Kim, H.-J. Sohn, *Energy Environ. Sci.* **2011**, *4*, 1986.
- [3] C.-M. Park, J.-H. Kim, H. Kim, H.-J. Sohn, *Chem. Soc. Rev.* **2010**, *39*, 3115.
- [4] D. Liu, Z. jiao Liu, X. Li, W. Xie, Q. Wang, Q. Liu, Y. Fu, D. He, *Small* **2017**, *13*, 1702000.
- [5] X. Su, Q. Wu, J. Li, X. Xiao, A. Lott, W. Lu, B. W. Sheldon, J. Wu, *Adv. Energy Mater.* **2014**, *4*, 1300882.
- [6] S. Liu, L. Kang, J. Zhang, S. C. Jun, Y. Yamauchi, *ACS Energy Lett.* **2021**, *6*, 4127.
- [7] Z. Liu, Q. Yu, Y. Zhao, R. He, M. Xu, S. Feng, S. Li, L. Zhou, L. Mai, *Chem. Soc. Rev.* **2019**, *48*, 285.
- [8] H. Yang, T. Xiong, Z. Zhu, R. Xiao, X. Yao, Y. Huang, M.-S. Balogun, *Carbon Energy* **2022**, *4*, 820.

- [9] S. Zhou, P. Huang, T. Xiong, F. Yang, H. Yang, Y. Huang, D. Li, J. Deng, M. S. Balogun, *Small* **2021**, *17*, 2100778.
- [10] Y. Reynier, C. Vincens, C. Leys, B. Amestoy, E. Mayousse, B. Chavillon, L. Blanc, E. Gutel, W. Porcher, T. Hirose, C. Matsui, *J. Power Sources* **2020**, *450*, 227699.
- [11] B. A. Boukamp, G. C. Lesh, R. A. Huggins, *J. Electrochem. Soc.* **1981**, *128*, 725.
- [12] M. N. Obrovac, L. Christensen, *Electrochim. Solid-State Lett.* **2004**, *7*, A93.
- [13] S. C. Jung, J. W. Choi, Y.-K. Han, *Nano Lett.* **2012**, *12*, 5342.
- [14] J. K. Lee, C. Oh, N. Kim, J.-Y. Hwang, Y.-K. Sun, *J. Mater. Chem. A* **2016**, *4*, 5366.
- [15] T. Chen, J. Wu, Q. Zhang, X. Su, *J. Power Sources* **2017**, *363*, 126.
- [16] H. Li, H. Li, Z. Yang, L. Yang, J. Gong, Y. Liu, G. Wang, Z. Zheng, B. Zhong, Y. Song, Y. Zhong, Z. Wu, X. Guo, *Small* **2021**, *17*, 2102641.
- [17] B.-C. Yu, Y. Hwa, C.-M. Park, H.-J. Sohn, *J. Mater. Chem. A* **2013**, *1*, 4820.
- [18] J.-Y. Li, Q. Xu, G. Li, Y.-X. Yin, L.-J. Wan, Y.-G. Guo, *Mater. Chem. Front.* **2017**, *1*, 1691.
- [19] D. J. Chung, D. Youn, S. Kim, D. Ma, J. Lee, W. J. Jeong, E. Park, J.-S. Kim, C. Moon, J. Y. Lee, H. Sun, H. Kim, *Nano Energy* **2021**, *89*, 106378.
- [20] J. Han, S. Jo, I. Na, S. Oh, Y. Jeon, J. Park, B. Koo, H. Hyun, S. Seo, D. Lee, H. Kim, J. Kim, J. Lim, J. Lim, *ACS Appl. Mater. Interfaces* **2021**, *13*, 52202.
- [21] N. Lin, Y. Han, J. Zhou, K. Zhang, T. Xu, Y. Zhu, Y. Qian, *Energy Environ. Sci.* **2015**, *8*, 3187.
- [22] M. Nagamori, I. Malinsky, A. Claveau, *Metall. Trans. B* **1986**, *17*, 503.
- [23] H. Nara, T. Yokoshima, T. Momma, T. Osaka, *Energy Environ. Sci.* **2012**, *5*, 6500.
- [24] Y. Tan, T. Jiang, G. Z. Chen, *Front. Energy Res.* **2021**, *9*.
- [25] A. Raza, J. Y. Jung, C.-H. Lee, B. G. Kim, J.-H. Choi, M.-S. Park, S.-M. Lee, *ACS Appl. Mater. Interfaces* **2021**, *13*, 7161.
- [26] B. Liu, J. Liu, C. Zhong, W. Hu, *Carbon Energy* **2024**, *6*, e421.
- [27] Y. Zhang, G. Guo, C. Chen, Y. Jiao, T. Li, X. Chen, Y. Yang, D. Yang, A. Dong, *J. Power Sources* **2019**, *426*, 116.
- [28] J. Wang, X. Wang, B. Liu, H. Lu, G. Chu, J. Liu, Y.-G. Guo, X. Yu, F. Luo, Y. Ren, L. Chen, H. Li, *Nano Energy* **2020**, *78*, 105101.
- [29] X. H. Liu, L. Zhong, S. Huang, S. X. Mao, T. Zhu, J. Y. Huang, *ACS Nano* **2012**, *6*, 1522.
- [30] M. T. McDowell, S. W. Lee, W. D. Nix, Y. Cui, *Adv. Mater.* **2013**, *25*, 4966.
- [31] D. Youn, N. G. Kim, W. J. Jeong, D. J. Chung, J. Y. Kim, H. Kim, *ACS Appl. Mater. Interfaces* **2022**, *14*, 45333.
- [32] J. Wu, Q. Dong, Q. Zhang, Y. Xu, X. Zeng, Y. Yuan, J. Lu, *Adv. Mater.* **2024**, *36*, 2405751.
- [33] H.-R. Yang, J. Hwang, H. Seo, K. Kim, J.-H. Kim, *J. Power Sources* **2022**, *519*, 230777.
- [34] Y. Cao, J. C. Bennett, R. A. Dunlap, M. N. Obrovac, *Chem. Mater.* **2018**, *30*, 7418.
- [35] J. Tang, L. Hou, T. Hu, S. Fan, X. Zhou, J. Yang, *Compos. Commun.* **2021**, *23*, 100544.
- [36] X. Meng, H. Huo, Z. Cui, X. Guo, S. Dong, *Electrochim. Acta* **2018**, *283*, 183.
- [37] J. Yang, *Solid State Ion.* **2002**, *152*–153, 125.
- [38] L. Zhang, J. Deng, L. Liu, W. Si, S. Oswald, L. Xi, M. Kundu, G. Ma, T. Gemming, S. Baunack, F. Ding, C. Yan, O. G. Schmidt, *Adv. Mater.* **2014**, *26*, 4527.
- [39] R. J. Temkin, *Journal of Non-Cryst. Solids* **1975**, *17*, 215.
- [40] A. I. Freytag, A. D. Pauric, M. Jiang, G. R. Goward, *J. Phys. Chem. C* **2019**, *123*, 11362.
- [41] J. E. Entwistle, S. V. Patwardhan, *RSC Adv.* **2021**, *11*, 3801.
- [42] M. Jana, D. Das, A. K. Barua, *Solar Energy Mater. Solar Cells* **2002**, *74*, 407.
- [43] G. Xiao-Yong, Z. Jian-Tao, L. Yu-Fen, L. Qing-Geng, C. Yong-Sheng, G. Jin-Hua, Y. Shi-E, L. Jing-Xiao, *Acta Phys. Pol. A* **2009**, *115*, 738.
- [44] T. D. Shen, C. C. Koch, T. L. McCormick, R. J. Nemanich, J. Y. Huang, J. G. Huang, *J. Mater. Res.* **1995**, *10*, 139.
- [45] P. Unifantowicz, S. Vaucher, M. Lewandowska, K. J. Kurzydłowski, *J. Phys.: Condens. Matter* **2007**, *20*, 025205.
- [46] W.-R. Liu, Y.-C. Yen, H.-C. Wu, M. Winter, N.-L. Wu, *J. Appl. Electrochem.* **2009**, *39*, 1643.
- [47] Z.-L. Wu, S.-B. Ji, L.-K. Liu, T. Xie, L. Tan, H. Tang, R.-G. Sun, *Rare Met.* **2021**, *40*, 1110.
- [48] J. Li, J. R. Dahn, *J. Electrochem. Soc.* **2007**, *154*, A156.
- [49] K. Ogata, E. Salager, C. J. Kerr, A. E. Fraser, C. Ducati, A. J. Morris, S. Hofmann, C. P. Grey, *Nat. Commun.* **2014**, *5*, 3217.
- [50] A. Hohl, T. Wieder, P. A. Van Aken, T. E. Weirich, G. Denninger, M. Vidal, S. Oswald, C. Deneke, J. Mayer, H. Fuess, *J. Non-Cryst. Solids* **2003**, *320*, 255.

Manuscript received: June 20, 2025

Revised manuscript received: August 6, 2025

Version of record online: